RSC Advances

PAPER

View Article Online
View Journal | View Issue

Open Access Article. Published on 02 January 2026. Downloaded on 1/20/2026 9:03:54 PM.
This article is licensed under a Creative Commons Attribution-NonCommercial 3.0 Unported Licence.

Check for updates

Cite this: *RSC Adv.*, 2026, **16**, 394

Liposome nanoparticles with photothermal effect for the treatment of bacterial infectious periodontitis

Juan Zhang,†*[ab] Qing Yang,†[ab] Cailing Zhao,[ab] Shisheng Cao,[c] Meng Xia,[ab] Xingtong Mu[ab] and Huijuan Yin*[c]

A novel strategy is imperative to address the limitations of conventional mechanical and pharmacological periodontal treatments, which are constrained by the inherent difficulty in completely eradicating plaque biofilm and the tendency for bacterial resistance to develop. Photothermal therapy (PTT) emerges as an innovative therapeutic approach for managing periodontitis, offering the distinct advantage of circumventing drug resistance. Furthermore, Near-Infrared-II (NIR-II) guided PTT enhances therapeutic efficacy and provides a viable method for eliminating bacteria in deep periodontal pockets. In this study, we encapsulated 2TT-oC6B, a fluorophore with aggregation-induced emission (AIE) properties, into liposomes to make AIE nanoparticles (2TT-oC6B@LIP), thereby improving their water dispersibility and enabling their use as photothermal agents for treating periodontitis. Upon exposure to 808 nm NIR irradiation, 2TT-oC6B@LIP effectively eradicated a broad spectrum of periodontal pathogens, including both Gram-positive *Streptococcus gordonii* (*S. gordonii*) and Gram-negative *Porphyromonas gingivalis* (*P. gingivalis*). Post-PTT treatment with 2TT-oC6B@LIP resulted in significant damage to bacterial cell membranes, cytoplasmic leakage, and potent anti-biofilm activity against periodontal pathogens. Additionally, an experimental periodontitis model was established in Sprague-Dawley (SD) rats, and the application of 2TT-oC6B@LIP significantly mitigated the progression of periodontitis under NIR light irradiation at an intensity of 1 W cm^{-2}. 2TT-oC6B@LIP nanoparticles exhibit remarkable photothermal bactericidal efficacy and good biocompatibility, offering promising potential for periodontitis therapy.

Received 27th October 2025
Accepted 9th December 2025

DOI: 10.1039/d5ra08225k

rsc.li/rsc-advances

1. Introduction

Periodontitis represents a significant global public health challenge, with a prevalence reaching up to 50% and an escalating incidence.[1,2] This chronic inflammatory disease, primarily caused by bacterial infection, can lead to chronic pain, destruction of periodontal supportive tissues, and tooth loss if left untreated or inadequately managed.[3–5] The key etiological agents of periodontitis include *S. gordonii* and *P. gingivalis*.[6–8] Current treatment modalities can partially reduce the microbial load in periodontal tissues.[9,10] However, the periodontium's complex anatomy hinders mechanical treatments from fully eradicating deep-seated bacteria, while prolonged medication use risks adverse effects and bacterial resistance.[11,12] Thus, there is an urgent need for more effective strategies to combat periodontal infections, remove biofilms, and prevent bacterial resistance.

Near-infrared (NIR) photothermal therapy (PTT) is a new strategy to combat bacterial infections. PTT uses photothermal agents (PTAs) to convert light into heat, targeting specific areas. This process ruptures bacterial membranes, leaks cytoplasmic components, and denatures proteins, effectively killing bacteria and removing biofilms. PTT offers excellent tissue penetration and avoids drug resistance.[13–15] Various PTAs have been studied, including noble metals,[16,17] metal sulfides,[18–20] metal oxides,[21,22] carbon-based materials,[23,24] polymers,[25,26] and organic small molecules.[27] While effective against *S. aureus* and *E. coli*, research on periodontal-resistant bacteria is limited.[28,29] Traditional PTAs face issues like aggregation-induced quenching(ACQ), low efficiency, poor stability, long retention, and low biosafety, limiting their clinical use.[30] Developing more effective PTAs to target periodontal-resistant strains is urgently needed.

In 2001, Tang Benzhong's team discovered aggregation-induced emission (AIE), where AIE fluorogens (AIEgens) emit weak or no light in dilute solutions but strong fluorescence when aggregated.[31–33] 2TT-oC6B, a novel NIR-II AIE material, offers deeper tissue penetration and better tissue tolerance in the NIR-II

[a]*Department of Prosthodontics, Tianjin Medical University School and Hospital of Stomatology & Tianjin Key Laboratory of Oral Soft and Hard Tissues Restoration and Regeneration, No. 12 Qixiangtai Road, Heping District, Tianjin 300070, PR China. E-mail: kqzhangjuan@126.com*

[b]*Tianjin Medical University Institute of Stomatology, No. 12 Qixiangtai Road, Heping District, Tianjin 300070, PR China. E-mail: kqzhangjuan@126.com*

[c]*Chinese Academy of Medical Sciences, Peking Union Medical College Institute of Biomedical Engineering, Tianjin, 300192, PR China. E-mail: yinhj@bme.pumc.edu.cn*

† These authors contributed equally to this work.

© 2026 The Author(s). Published by the Royal Society of Chemistry

Open Access Article. Published on 02 January 2026. Downloaded on 1/20/2026 9:03:54 PM.
This article is licensed under a Creative Commons Attribution-NonCommercial 3.0 Unported Licence.

range (1000–1700 nm).[34–36] Its high signal-to-noise ratio (SBR) and NIR-II imaging capabilities enable intraoperative ureter identification and brain inflammation imaging.[37,38] However, its use in photothermal therapy is underexplored. To investigate its photothermal potential, a liposome-encapsulated 2TT-oC6B nanodelivery system was developed. Liposomes are highly biocompatible due to their natural presence in cell membranes. They can encapsulate hydrophobic and hydrophilic drugs, improving solubility.[39–41] As drug carriers, liposomes protect molecules from degradation and extend their half-life.[42,43] Surface modification with polyethylene glycol (PEG) further enhances their *in vivo* circulation time.[44]

This study developed liposome nanoparticles (2TT-oC6B@LIP) with NIR-II and AIE properties by encapsulating 2TT-oC6B into liposome bilayers with hydrophilic PEG chains, achieving good water dispersion. The 2TT-oC6B@LIP showed a high photothermal conversion efficiency (68.4%) under NIR irradiation (1 W cm^{-2}, 5 minutes). *In vitro*, it effectively eliminated periodontal bacteria (*S. gordonii* and *P. gingivalis*) and their biofilms. *In vivo* studies using a periodontitis model in SD rats confirmed its significant therapeutic effects, demonstrating the potential of NIR-II AIEgens for treating periodontitis (Scheme 1).

2. Experimental section

2.1 Main materials

Nankai University generously provided 2TT-oC6B. Phospholipids (DPPC), cholesterol (Chol), and Distearoyl Phosphatidylcholine – Polyethylene Glycol 2000(DSPE-PEG_{2000}) were procured from Xi'an Rui Xi Biological Technology Co., Ltd (Xi'an, China). The Cell Counting Kit-8 (CCK-8), Acridine Orange/Ethidium Bromide (AO/EB),*o*-nitrophenyl-β-D-galactopyranoside (ONPG) assay, the Bicinchoninic Acid Assay(BCA) protein assay kit, and Calcein AM/PI Double Staining Kit were supplied by Beyotime Biotechnology Co., Ltd (Beijing, China). Indocyanine green and Phosphate-buffered saline (PBS) were obtained from J&K Scientific Co., Ltd (Beijing, China).

2.2 Bacterial and cell culture

The two periodontal pathogens used in this study were *S. gordonii* (ATCC 10558), a representative Gram-positive bacterium, and *P. gingivalis* (BNCC 353909), a Gram-negative bacterium. *S. gordonii* was provided by the laboratory of the Stomatological Hospital of Tianjin Medical University, China, while *P. gingivali* was purchased from Suzhou BeiNaChuangLian Biotechnology Co. *P. gingivalis* was cultured in brain heart infusion (BHI) broth supplemented with hemoglobin chloride (5 mg L^{-1}), vitamin K (1 mg L^{-1}), and 5% defibrinated sheep blood (which was purchased from Qingdao Haibo Biotechnology Co., Ltd, model number 1001339-1)at 37 °C under anaerobic conditions (80% N_2, 10% H_2, and 10% CO_2). *S. gordonii* was grown in BHI broth at 37 °C under aerobic conditions with 5% CO_2. Both bacteria were cultured to the logarithmic growth phase, reaching a concentration of approximately 1×10^8 CFU ml^{-1}, for subsequent single-strain biofilm formation and antimicrobial experiments.

Mouse fibroblasts (L929) were obtained from the Tianjin Medical University Stomatological Hospital. The L929 cells were cultured in Dulbecco's Modified Eagle Medium (DMEM)

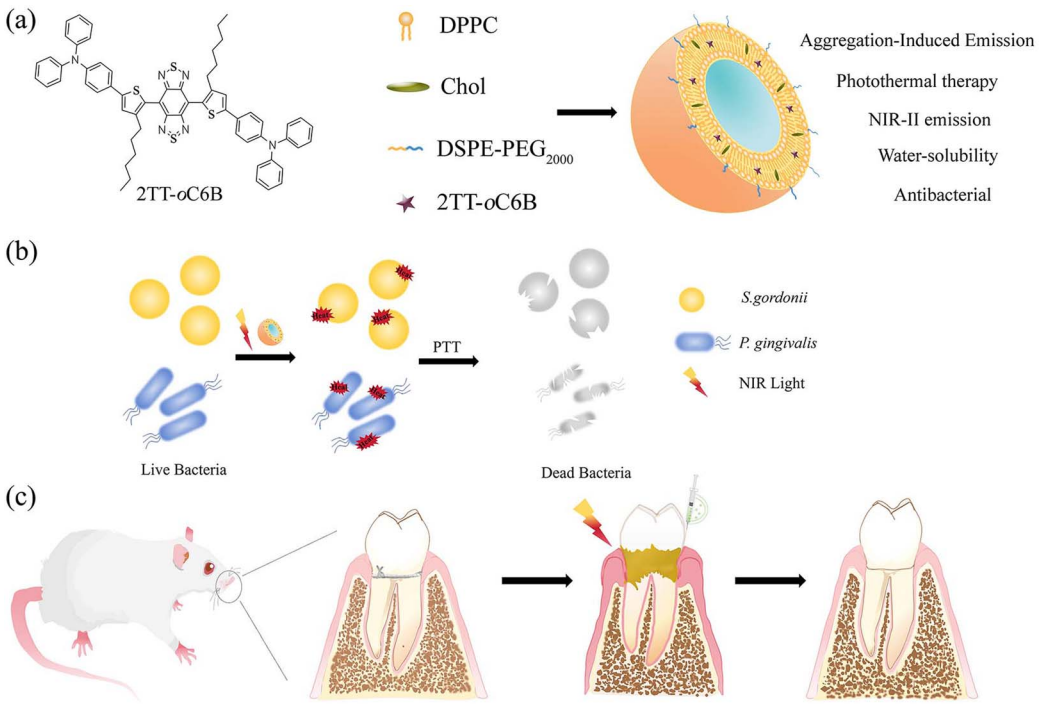

Scheme 1 Schematic illustration of the 2TT-oC6B@LIP for periodontitis treatment. (a) Preparation of 2TT-oC6B@LIP. (b)The antibacterial ability of capacity of 2TT-oC6B@LIP + L *in vitro*. (c) To investigate the effectiveness of the 2TT-oC6B@LIP + L in periodontitis, an experimental model of periodontitis in SD rats was established to evaluate the antibacterial efficacy of 2TT-oC6B@LIP + L *in vivo*.

Open Access Article. Published on 02 January 2026. Downloaded on 1/20/2026 9:03:54 PM. This article is licensed under a Creative Commons Attribution-NonCommercial 3.0 Unported Licence.

supplemented with 10% fetal bovine serum (FBS) and 1% penicillin/streptomycin, and maintained at 37 °C in a humidified atmosphere containing 5% CO_2 for 24 hours.

2.3 Preparation of liposomal nanoparticles (2TT-oC6B@LIP)

2TT-oC6B@LIP was prepared using the nano-precipitation method. Specifically, DPPC, Chol, DSPE-PEG_{2000}, and 2TT-oC6B (in a mass ratio of 6 : 3 : 1 : 1) were weighed and dissolved in 1 ml of a mixed solution of anhydrous ethanol and tetrahydrofuran (THF) (1 : 1, v/v)at room temperature. Vortex the mixture until it is completely dissolved. This solution was then added dropwise to 10 ml of deionized water under continuous stirring. The resulting mixture was sonicated for 5 minutes at 35% power using a probe sonication system while maintained in an ice bath (0–4 °C) to prevent overheating. The 2TT-oC6B@LIP solution, after ultrasonic treatment, was transferred into a dialysis bag (MWCO: 14 kDa) and dialyzed at room temperature for 24 h under stirring at 200 rpm to remove residual anhydrous ethanol and THF. The purified suspension was collected to obtain the final 2TT-oC6B@LIP product. All experimental steps were carried out under light-protected conditions.

2.4 Characterization

The micromorphology of 2TT-oC6B@LIP was examined using transmission electron microscopy (TEM, Hitachi HT7700, Tokyo, Japan). The size distribution and dispersion of 2TT-oC6B@LIP were analyzed using dynamic light scattering (DLS) with a particle size analyzer. The particle size and polydispersity index (PDI) were monitored over seven consecutive days to evaluate the *in vitro* stability of 2TT-oC6B@LIP. The ultraviolet-visible (UV-vis) absorption spectrum of 2TT-oC6B@LIP was measured using a UV-vis spectrophotometer (U-3900, Japan). A standard curve for 2TT-oC6B was established by measuring the absorbance at 808 nm for a series of 2TT-oC6B solutions at different concentrations (50, 25, 12.5, 6.25, and 3.125 μg ml^{-1}). Based on this, the Encapsulation Efficiency(EE) and Drug Loading(DL) capacity of 2TT-oC6B@LIP were calculated using the following formulas:

$$\text{EE } (\%) = \frac{\text{Mass of encapsulated 2TT-oC6B}}{\text{Total mass of 2TT-oC6B added}} \times 100\% \quad (1)$$

$$\text{DL } (\%) = \frac{\text{Mass of encapsulated 2TT-oC6B}}{\text{Total mass of liposomes}} \times 100\% \quad (2)$$

The functional groups of 2TT-oC6B@LIP and 2TT-oC6B were characterized using Fourier transform infrared spectroscopy (FT-IR, Japan).

2.5 Evaluation of photothermal performance of 2TT-oC6B@LIP

An 808 nm NIR laser diode (Beijing Viasho Technology Co., Ltd) with a spectral Full Width at Half Maximum(FWHM) of <3 nm was used for photothermal irradiation. The beam was collimated to a 2.5 mm^2 spot on the sample, and the output power was calibrated with a Gentec-EO Maestro series power meter to ensure a uniform power density of 1.0 W cm^{-2} across all treatments. To investigate the photothermal properties of 2TT-oC6B@LIP, 200 μl of 2TT-oC6B@LIP (100 μg ml^{-1}) was irradiated with NIR light at different power densities (0.5, 0.6, 0.7, 0.8, 0.9, and 1 W cm^{-2}) for 10 minutes. Additionally, 200 μl of phosphate-buffered saline (PBS) (as a control) and 2TT-oC6B@LIP at various concentrations (75, 50, and 25 μg ml^{-1}) were irradiated with near-infrared (NIR) light (1 W cm^{-2}) for 10 minutes. The temperature changes of 2TT-oC6B@LIP were monitored using a thermocouple probe at 30-second intervals. Following the photothermal response analysis, subsequent experiments utilized 2TT-oC6B@LIP (50 μg ml^{-1}) with 808 nm NIR irradiation (1 W cm^{-2}, 5 min). The photothermal stability of ICG and 2TT-oC6B@LIP was evaluated through ON/OFF cycling experiments under NIR irradiation. Specifically, ICG and 2TT-oC6B@LIP were exposed to NIR light (1 W cm^{-2}), followed by natural cooling to the initial temperature. This process was repeated for three cycles to assess the stability and reproducibility of the photothermal effect. The warming and cooling temperature trends of 2TT-oC6B@LIP (50 μg ml^{-1}) were recorded using a thermocouple probe. Finally, the photothermal conversion efficiency (η) of 2TT-oC6B@LIP was calculated using the following equation.

$$\eta = \frac{hS(T_{\max} - T_{\text{surr}}) - Q_{\text{Dis}}}{\text{I}\left(1 - 10^{-A\lambda}\right)} \quad (3)$$

$$\tau_s = \frac{m_d C_d}{hS} \quad (4)$$

$$Q_{\text{Dis}} = \frac{m_d C_d (T_{\max} - T_{\text{surr}})}{t} \quad (5)$$

In the equation, h represents the thermal conductivity, S denotes the surface area of the vessel, and τ_s is derived from the linear regression curve during the cooling process. $T_{\max}$ signifies the maximum temperature at which the 2TT-oC6B@LIP stabilizes, while T_{surr} indicates the ambient temperature. Q_{Dis} represents the heat loss of the water as it absorbs light. m_d and C_d refer to the mass of the solvent (1 g) and the specific heat capacity of the solvent (4.2 J g^{-1} K^{-1}), respectively. The variable t corresponds to the time required for the water to reach the maximum temperature difference. The parameter i represents the laser power, and A^{λ} represents the absorbance of 2TT-oC6B@LIP at 808 nm.

2.6 Measurement of colony-forming units (CFU)

Following the bacterial culture methods described above, the experiments were divided into four groups:

(1) Control group: treated with PBS only;

(2) Control + L group: treated with PBS and irradiated with NIR light (1 W cm^{-2} × 100%) for 5 minutes;

(3) 2TT-oC6B@LIP group: treated with 2TT-oC6B@LIP only;

(4) 2TT-oC6B@LIP + L group: treated with 2TT-oC6B@LIP and irradiated with NIR light (1 W cm^{-2}) for 5 minutes.

The antimicrobial properties of 2TT-oC6B@LIP were evaluated using the plate coating method. Bacterial suspensions of *S. gordonii* and *P. gingivalis* were centrifuged and washed three

 © 2026 The Author(s). Published by the Royal Society of Chemistry

Open Access Article. Published on 02 January 2026. Downloaded on 1/20/2026 9:03:54 PM. This article is licensed under a Creative Commons Attribution-NonCommercial 3.0 Unported Licence.

times with PBS to remove residual macromolecules. The supernatant was discarded, and the bacterial pellets were treated with the four different treatments mentioned above (PBS, PBS + L, 2TT-oC6B@LIP, and 2TT-oC6B@LIP + L). The mixtures were co-incubated at 37 °C for 2 hours with gentle shaking at 100 rpm. After incubation, the samples were centrifuged at 6000 rpm and washed three times with PBS.

Subsequently, the bacterial suspensions from each group were serially diluted and transferred to a 96-well plate. Aliquots of 10 μl from each dilution were spread evenly onto CDC anaerobic agar plates (for *P. gingivalis*) and BHI agar plates (for *S. gordonii*). The plates were incubated under the respective conditions described above. After single colonies formed, the bacterial survival rate for each group was calculated based on the colony counts. Each experiment was performed in triplicate.

$$\text{Antibacterial rate } (\%) = \frac{(A_1 - A_2)}{A_1} \times 100\% \quad (6)$$

A_1 denotes the mean colony count for the control group, while A_2 represents the mean bacterial colony count for the experimental group.

2.7 Morphological observation of bacteria

The morphology of *S. gordonii* and *P. gingivalis* was observed using scanning electron microscopy (SEM) and transmission electron microscopy (TEM). Bacterial suspensions of *S. gordonii* and *P. gingivalis* were co-incubated with 1 ml of the different treatment groups mentioned above for 2 hours. For the light-treated groups, the samples were irradiated with NIR light (1 W cm^{-2}) for 5 minutes. After treatment, each sample group was fixed with 2.5% glutaraldehyde for 4 hours at room temperature. The fixed samples were washed three times with PBS and then dehydrated using a series of gradient ethanol solutions (30%, 50%, 70%, 80%, 90%, and 100%, each for 15 minutes). Following dehydration, the samples were sputter-coated with gold and observed under a scanning electron microscope to examine the morphology of *S. gordonii* and *P. gingivalis*.

For TEM analysis, the two bacterial species were treated separately using the same method described above. A 20 μl aliquot of each bacterial suspension was drop-cast onto carbon-coated 200-mesh copper grids and allowed to dry. The grids were then examined using TEM to observe the ultrastructure of the bacteria.

2.8 Assessment of bacterial outer membrane integrity

To further investigate bacterial membrane permeability and bacterial protein leakage, the ONPG assay and the BCA protein assay kit were employed. For the ONPG assay, 3.75 mg of ONPG (0.25 mM) was weighed and dissolved in 500 μl of PBS. A 100 μl aliquot of *S. gordonii* or *P. gingivalis* bacterial suspension was added to a 96-well plate and incubated with the respective treatment groups for 2 hours, following the experimental grouping scheme described above. After incubation, 100 μl of the bacterial suspension was transferred to a new 96-well plate and reacted with 10 μl of the ONPG assay reagent for 30 minutes. The absorbance at 420 nm was measured using a microplate reader.

For the BCA protein assay, a working solution was prepared by mixing 3 ml of BCA reagent with 60 μl of Cu reagent at a ratio of 50 : 1. A 100 μl aliquot of each bacterial suspension was co-incubated with the respective treatment groups for 2 hours, followed by light treatment as appropriate. The bacterial suspensions were then centrifuged, and 20 μl of the supernatant from each group was added to 200 μl of the BCA working solution. The mixture was incubated at 37 °C for 30 minutes in the dark, and the absorbance at 562 nm was measured using a microplate reader.

2.9 Evaluation of anti-bacterial biofilm effects

1 ml of *S. gordonii* or *P. gingivalis* suspension was transferred to a confocal dish and incubated in the dark for 3 or 5 days, respectively, to form mature biofilms. After incubation, the suspension was discarded, and biofilms were co-incubated with 1 ml of PBS or 2TT-oC6B@LIP for 2 hours. Biofilms were then stained with Calcein Acetoxymethyl (Calcein-AM) and Propidium Iodide (PI) for 30 minutes in the dark, washed with PBS, and observed under confocal microscopy.

For 24-well plates, 1 ml of *S. gordonii* and *P. gingivalis* suspensions was cultured under optimal conditions (3 days for *S. gordonii*, 5 days for *P. gingivalis*) to form biofilms, with daily medium refreshment. After biofilm formation, suspensions were aspirated, and biofilms were rinsed with PBS and co-incubated with 1 ml of PBS or 2TT-oC6B@LIP for 6 hours. The light-treated group received NIR irradiation (1 W cm^{-2}, 5 minutes). Biofilms were fixed with 2.5% glutaraldehyde for 20 minutes, air-dried, stained with 0.1% crystal violet for 20 minutes, rinsed, and air-dried again. Decolorization was performed with 95% ethanol for 5 minutes, and absorbance at 600 nm was measured using a microplate reader.

2.10 Cytotoxicity assay

L929 cells were seeded at a density of 1×10^4 cells per well in a 24-well plate and treated with 2TT-oC6B@LIP and 2TT-oC6B@LIP + L (50, 25, 12.5, 6.25 μg ml^{-1}), DMEM (Control), and DMEM + L (Control + L), respectively. Only the groups designated for light treatment received laser irradiation, as previously described. Cells were incubated as described above for 1, 3, 5, and 7 days, with daily medium replacement. After incubation, 500 μl of fresh medium with 10% CCK-8 reagent was added and incubated for 1 hour. Cell viability was measured at 450 nm using a microplate reader.

In another experiment, L929 cells were seeded at a density of 1×10^4 cells per well and cultured with 1 ml of 2TT-oC6B@LIP and 2TT-oC6B@LIP + L (at concentrations of 50, 25, 12.5, and 6.25 μg ml^{-1}), DMEM, and DMEM + L for 1 and 3 days. After incubation, the supernatant was discarded, cells were rinsed with PBS, and stained with AO/EB for 30 minutes in the dark. Excess dye was removed with PBS, and fluorescence imaging was performed using an inverted fluorescence microscope.

Blood was collected from SD rats' abdominal aorta, and the red blood cells (RBCs) were isolated to prepare a 5% RBC

Open Access Article. Published on 02 January 2026. Downloaded on 1/20/2026 9:03:54 PM. This article is licensed under a Creative Commons Attribution-NonCommercial 3.0 Unported Licence.

suspension in PBS, stored at 4 °C. For the hemolysis assay, 500 μl of 1% Triton-X 100 (positive control) and PBS (negative control) were set up under both light-exposed and non-light-exposed conditions. Different concentrations of 2TT-oC6B@LIP and 2TT-oC6B@LIP + L(50, 25, 12.5, 6.25 μg ml^{-1}) were mixed 1 : 1 (v/v) with the RBC suspension, incubated at 37 °C for 4 hours, and centrifuged at 1500 rpm for 10 minutes. The supernatant's absorbance was measured at 540 nm using a microplate reader. The hemolysis rate was calculated using OD values with the formula:

$$\text{Hemolysis ratio } (\%) = \frac{A_M - A_N}{A_P - A_N} \times 100 \quad (7)$$

A_M, A_N, and A_p represent the absorbance of each experimental group, the Control group, and Triton-X, respectively.

2.11 Treatment of experimental periodontitis in rats by 2TT-oC6B@LIP *in vitro*

All animal-related procedures were conducted in compliance with the Regulations on the Management of Experimental Animals of Tianjin Medical University and were approved by the Animal Ethics Committee of the Institute of Radiation Medicine, Chinese Academy of Medical Sciences (approval no: IRM/2-IACUC-2503-040). Twenty male SD rats (260–300 g) were provided by Beijing Viton Lihua Laboratory Animal Technology Co., Ltd. Before surgery, the rats were fasted and dehydrated for 12 hours. Anesthesia was induced by intraperitoneal injection of sodium pentobarbital (2%, 0.3 ml/100 g body weight). A mechanical and bacterial stimulation-induced periodontal inflammation model was established as follows: after anesthesia, orthodontic ligature wires were placed below the gingiva of the maxillary second molar and tied buccally around the anterior aspect of the maxillary first molar. The gingival region was then inoculated with 20 μl of a 1 : 1 mixture of *S. gordonii* and *P. gingivalis* to induce periodontitis. The rats were randomly divided into five groups ($n = 3$ per group):

Control group: no treatment was administered.

Periodontitis group: 20 μl of PBS was injected into the gingival sulcus.

2TT-oC6B@LIP group: 20 μl of 2TT-oC6B@LIP was injected into the gingival sulcus.

Minocycline hydrochloride group (Mino group): minocycline ointment was applied to the gingival sulcus.

2TT-oC6B@LIP + L group: 20 μl of 2TT-oC6B@LIP was injected into the gingival sulcus and incubated for 5 minutes, followed by irradiation with 808 nm NIR light at 1 W cm^{-2} for 5 minutes. A thermal imaging camera was used to monitor temperature changes in the periodontal area every minute. Treatments were administered weekly for three weeks.

Micro-CT imaging was performed on randomly selected rats before and after modeling to confirm the successful establishment of the periodontitis model. After four weeks of treatment, the rats were euthanized by overdose anesthesia. The maxillary alveolar bone was excised, rinsed with saline, and fixed in 4% paraformaldehyde for 48 hours. The samples were then scanned using a Micro-CT system (Bruker, Germany). The distance from the cementoenamel junction (CEJ) to the alveolar bone crest (ABC) was measured using CTVOX and CTan analysis software. Gingival tissues from the palatal side of the maxillary second molar were fixed in 4% paraformaldehyde, dehydrated through a graded ethanol series, embedded in paraffin, and sectioned for hematoxylin–eosin (H&E) and Masson staining.

To evaluate the biosafety of 2TT-oC6B@LIP, major organs (heart, liver, spleen, lungs, and kidneys) and blood samples were collected from each group. The organs were subjected to H&E staining, and blood samples were analyzed for biochemical parameters.

2.12 Statistical analyses

All the above experiments were repeated at least 3 times and were conducted under light protection. Statistical analyses were conducted using GraphPad Prism (GraphPad Software, USA). Specifically, one-way analysis of variance (ANOVA) followed by Tukey's *post hoc* test was employed to assess significant differences among groups. Results are expressed as mean ± standard deviation (SD). $P < 0.05$ indicates a statistically significant difference.

3. Results and discussion

3.1 Preparation and characterization of 2TT-oC6B@LIP

In this study, liposome-encapsulated NIR-II AIEgen was designed and synthesized using the nanoprecipitation method to eliminate periodontal drug-resistant bacterial infections through photothermal therapy. As shown in Figure.1(a), TEM images revealed that the nanoparticles exhibited a uniformly distributed spherical morphology. Fig. 1(b) demonstrates that the average particle size of 2TT-oC6B@LIP, as determined by dynamic light scattering (DLS), was 146.7 nm, with a polydispersity index (PDI) of 0.171. Fig. 1(c) shows that the particle size and PDI of 2TT-oC6B@LIP remained stable without significant fluctuations for 7 days, indicating excellent stability of the formulation. As illustrated in Fig. 1(d), the UV-vis absorption spectrum of 2TT-oC6B@LIP revealed strong absorption at 730 nm within the 300–1000 nm wavelength range. The encapsulation efficiency of 2TT-oC6B@LIP was calculated to be 87%, with a drug loading capacity of 8%, using the standard curve equation of 2TT-oC6B ($y = 0.0276x - 0.0009$, $R^2 = 0.9941$). As shown in Fig. 1(e) and (f), the temperature of 2TT-oC6B@LIP increased with both concentration and laser power during 10 min of NIR irradiation. The temperature change exhibited a rapid increase within the first five minutes, followed by stabilization in the last five minutes. At a concentration of 50 μg ml^{-1} under NIR irradiation for 5 min, the temperature of 2TT-oC6B@LIP exceeded 50 °C, which is sufficient to eliminate periodontal drug-resistant bacteria while preserving normal tissues.[45] Therefore, 50 μg ml^{-1} of 2TT-oC6B@LIP irradiated with NIR light at 1 W cm^{-2} for 5 min was selected for subsequent experiments. Three cycles of photothermal irradiation were conducted to evaluate the photothermal performance of 2TT-oC6B@LIP (Fig. 1(g)). Comparative studies with the photothermal agent indocyanine green (ICG) revealed that 2TT-oC6B@LIP maintained consistent

 © 2026 The Author(s). Published by the Royal Society of Chemistry

Open Access Article. Published on 02 January 2026. Downloaded on 1/20/2026 9:03:54 PM.
This article is licensed under a Creative Commons Attribution-NonCommercial 3.0 Unported Licence.

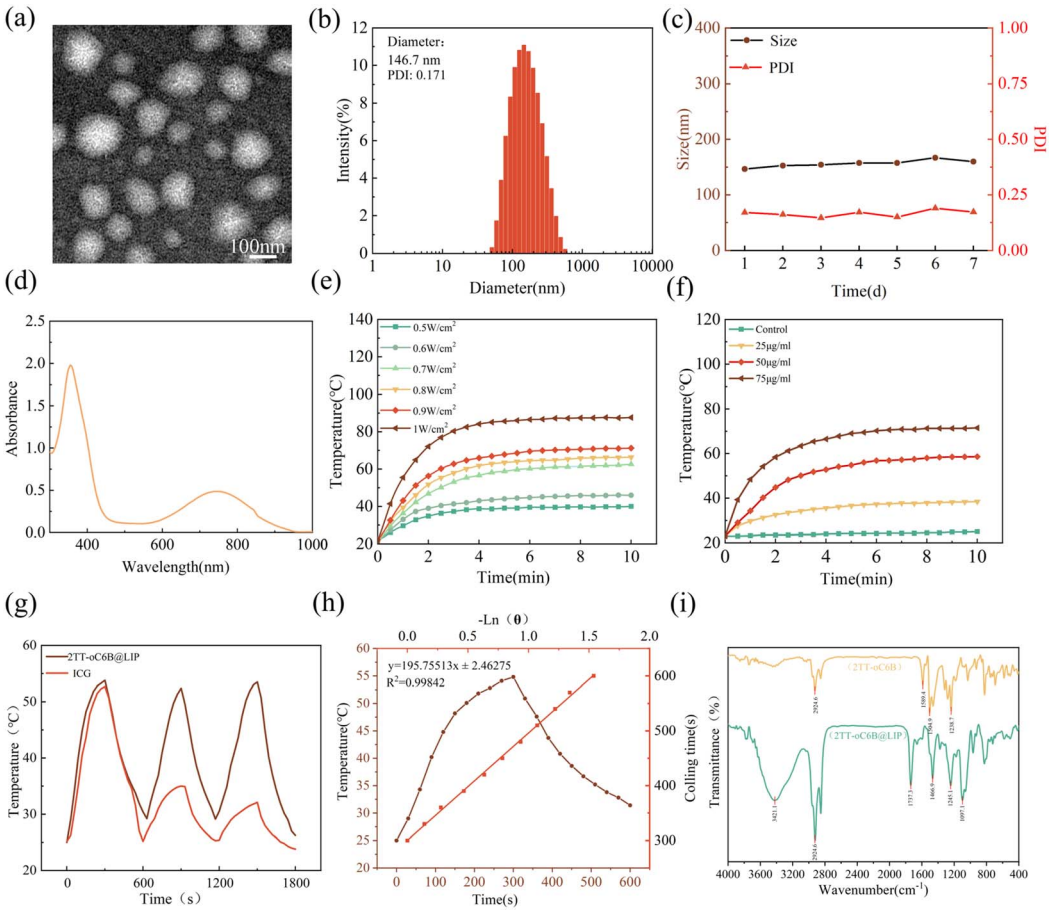

Fig. 1 Characterization of 2TT-oC6B@LIP.(a) TEM images of 2TT-oC6B@LIP, (b) hydrodynamic diameter distribution, (c) particle size and PDI of 7-day stability (d) UV-vis absorbance spectra of 2TT-oC6B@LIP. (e) Temperature variation curves of 2TT-oC6B@LIP (100 μg ml^{-1}) at different power densities. (f) Temperature variation curves of 2TT-oC6B@LIP (1.0 W cm^{-2}) at different concentrations. (g) Photothermal stability of 2TT-oC6B@LIP(50 μg ml^{-1}) under NIR light irradiation (808 nm, 1.0 W cm^{-2}) for 3 on/off cycles. (h) Photothermal performance of 2TT-oC6B@LIP (50 μg ml^{-1}), Brown line: photothermal effect. Red line: linear relationship between cooling time and −Ln(θ) for 2TT-oC6B@LIP. (i) FTIR spectra of 2TT-oC6B (yellow line) and 2TT-oC6B@LIP (green line).

temperature profiles across all cycles, demonstrating excellent photothermal stability and reproducibility. In contrast, ICG showed significant temperature fluctuations and a marked decrease in photothermal performance. Furthermore, based on the cooling curve analysis of 2TT-oC6B@LIP (Fig. 1(h)), the photothermal conversion efficiency was calculated to be 68.4%. The FTIR spectrum of 2TT-oC6B@LIP is shown in Fig. 1(i), displaying characteristic peaks at 3421 cm^{-1} (O–H stretching vibration), 1737 cm^{-1} (C=O stretching vibration), and 1466 cm^{-1} (CH_2 bending vibration). The IR bands at 1097 and 1245 cm^{-1} are characteristic of the phosphodiester bond in the phospholipid, confirming the presence of DPPC. Additionally, the absorption band at 2924 cm^{-1} corresponds to C–H stretching vibrations. The presence of these characteristic peaks confirms the successful preparation of 2TT-oC6B@LIP.

3.2 *In vitro* photothermal antimicrobial properties of 2TT-oC6B@LIP

To quantitatively assess the antibacterial efficacy, the colony-forming unit (CFU) assay was employed to determine the number of viable bacteria. Fig. 2(a–c) displays the agar plate images and antimicrobial rates of *S. gordonii* and *P. gingivalis* following different treatments. No significant difference in the number of colonies of *S. gordonii* and *P. gingivalis* was observed between the Control and Control + L groups ($P > 0.05$). In a dark environment, 2TT-oC6B@LIP increased the antimicrobial rates against *S. gordonii* and *P. gingivalis* to 25.8% ± 5.1% and 25.7% ± 7.5%, respectively. The antimicrobial rates against *S. gordonii* (100% ± 0%) and *P. gingivalis* (99.3% ± 0.9%) in the 2TT-oC6B@LIP + L group were significantly higher than those in the other groups ($P < 0.05$). The sharp reduction in CFU indicated that 2TT-oC6B@LIP possesses strong photothermal antibacterial properties.

3.3 Evaluation of bacterial morphology by TEM and SEM

Further observation of the morphological changes in *S. gordonii* and *P. gingivalis* after different treatments was conducted using SEM and TEM, with results consistent with previous antibacterial experiments. As shown in the TEM images in Fig. 2(d), *S. gordonii* exhibited an intact globular morphology, and *P. gingivalis* displayed

Open Access Article. Published on 02 January 2026. Downloaded on 1/20/2026 9:03:54 PM.
This article is licensed under a Creative Commons Attribution-NonCommercial 3.0 Unported Licence.

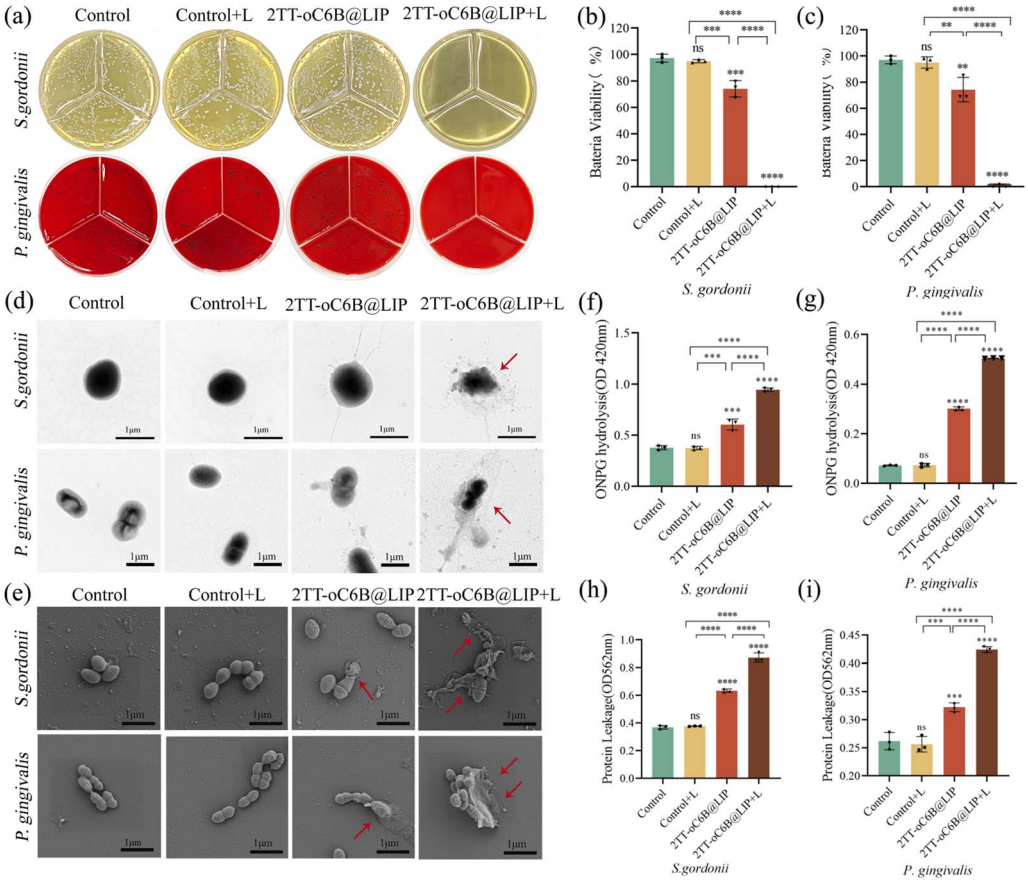

Fig. 2 *In vitro* antimicrobial effect of 2TT-oC6B@LIP.(a) Photographs of *S. gordonii* and *P. gingivalis* bacterial colonies following various treatments, accompanied by (b) and (c) the corresponding statistical histograms illustrating bacterial survival rates. (d) and (e) TEM and SEM images of *S. gordonii* and *P. gingivalis* after incubation under different treatment conditions. Red arrows indicate bacterial destruction, scale bar = 1 μm. (f) and (g) Results of the ONPG assay for *S. gordonii* and *P. gingivalis* subjected to different treatments. (h) and (i) BCA assay results quantifying protein leakage from *S. gordonii* and *P. gingivalis* under various treatment conditions. Data are presented as mean ± SD, $^{**}P < 0.01$, $^{***}P < 0.001$, $^{****}P < 0.0001$; ns denotes no significant difference.

a typical short-rod morphology in both the Control and Control + L groups, indicating that PBS does not affect bacterial morphology after light exposure. After treatment with 2TT-oC6B@LIP, a slight detachment of the cell wall and cell membrane was observed on the bacterial surface. In the 2TT-oC6B@LIP + L group, *S. gordonii* and *P. gingivalis* exhibited more pronounced damage to the cell membrane, leakage of the cytoplasm, and ultimately bacterial death. As shown in the SEM images in Fig. 2(e), the morphology of both bacteria appeared normal in the Control and Control + L groups. However, the bacterial morphology appeared crumpled and deformed after treatment with 2TT-oC6B@LIP. In the 2TT-oC6B@LIP + L group, the morphology of *S. gordonii* and *P. gingivalis* underwent more significant changes, with obvious collapse, crumpling, and near lysis of the bacteria, suggesting that photothermal action significantly enhances the antimicrobial effect.

3.4 Permeability and damage to bacterial cell membranes

The ONPG and BCA assays were employed to assess bacterial membrane integrity and protein leakage, respectively. Upon increased permeability of the bacterial cell membrane, ONPG underwent a reaction with intracellular β-D-galactosidase, leading to its hydrolysis into *o*-nitrophenol, which was subsequently quantified by measuring absorbance at 420 nm.[46,47] In the BCA assay, membrane damage leads to leakage of cytoplasmic proteins. Under alkaline conditions, these proteins reduce Cu^{2+} to Cu^{+}, which then forms a colored complex with BCA reagent. By quantifying the extracellular protein content *via* this method, we indirectly assess the extent of membrane damage. As depicted in Fig. 2(f) and (g), no statistically significant differences in absorbance values at 420 nm were observed between the Control and Control + L groups ($P > 0.05$). In contrast, a marked increase in OD420 nm values was noted in both 2TT-oC6B@LIP-treated groups ($P < 0.05$), with the 2TT-oC6B@LIP + L group exhibiting a particularly pronounced elevation in absorbance ($P < 0.05$). These data demonstrate that near-infrared light irradiation in the presence of 2TT-oC6B@LIP enhances the permeability of *S. gordonii* and *P. gingivalis* cell membranes, resulting in β-galactosidase leakage and consequent bacterial degradation.

The structural compromise of bacterial cell membranes facilitated the efflux of intracellular components, including proteins. As illustrated in Fig. 2(h) and (i), the OD562 nm measurements revealed no significant differences between the

 © 2026 The Author(s). Published by the Royal Society of Chemistry

Open Access Article. Published on 02 January 2026. Downloaded on 1/20/2026 9:03:54 PM.
This article is licensed under a Creative Commons Attribution-NonCommercial 3.0 Unported Licence.

Control and Control + L groups ($P > 0.05$). However, treatment with 2TT-oC6B@LIP significantly increased protein leakage from both *S. gordonii* and *P. gingivalis*. Notably, the 2TT-oC6B@LIP + L group exhibited the most substantial protein leakage ($P < 0.05$). These findings suggest that the bacterial cell membranes were severely damaged due to the photothermal effect of 2TT-oC6B@LIP, which accelerated the leakage of bacterial proteins.

3.5 Crystalline violet staining of bacterial biofilm

The extent of plaque biofilm removal significantly influences the outcomes of periodontitis treatment. To evaluate this, mature biofilms were first established and then subjected to the respective treatments. The remaining biofilm biomass was quantified using crystal violet staining, a method based on the dye's interaction with negatively charged surface molecules and polysaccharides in the biofilm's extracellular matrix, which imparts a dark violet coloration.[48] As depicted in Fig. 3(a) and (b), the Control and Control + L groups displayed a dark violet color, whereas the 2TT-oC6B@LIP + L group exhibited a lighter violet hue. Fig. 3(e) and (f) reveal that the biofilm biomass of *S. gordonii* and *P. gingivalis* in the Control + L group did not show a statistically significant difference ($P > 0.05$) compared to the Control group, indicating that PBS + L did not disrupt the biofilm of either bacterial species. The decrease in OD600 nm observed in the 2TT-oC6B@LIP group suggested that 2TT-oC6B@LIP caused some damage to the biofilms of both bacteria. Moreover, the reduction in OD600 nm was more pronounced in the 2TT-oC6B@LIP + L group, indicating that 2TT-oC6B@LIP + L induced transient yet highly efficient disruption of the *S. gordonii* and *P. gingivalis* biofilms, demonstrating a stronger capability in plaque biofilm removal ($P < 0.05$).

3.6 Bacterial biofilm live-dead staining

Fig. 3(c) and (d)illustrate that only green fluorescence was observed for *S. gordonii* and *P. gingivalis* in the Control and Control + L groups, suggesting that both bacterial strains were largely viable. In the 2TT-oC6B@LIP group, biofilm staining of *S. gordonii* and *P. gingivalis* revealed large areas of green

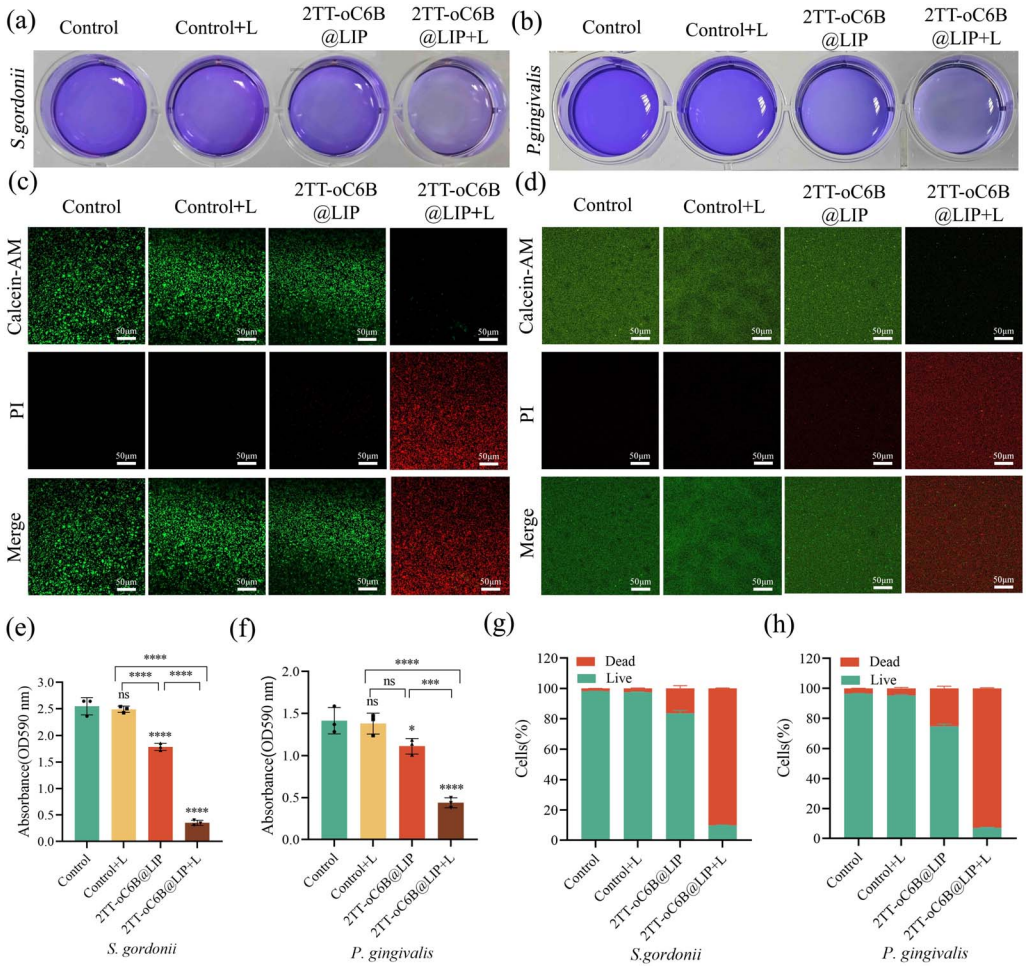

Fig. 3 *In vitro* anti-biofilm effect of 2TT-oC6B@LIP.Crystalline violet stained images of *S. gordonii* (a) and *P. gingivalis* (b) (c) Images of live-dead staining of *S. gordonii* biofilms, scale bar = 50 μm. (d) Images of live-dead staining of *P. gingivalis* biofilms, scale bar = 50 μm. Quantitative analysis of *S. gordonii* (e) and *P. gingivalis* (f) by crystal violet staining. Quantitative analysis of live-dead staining of *S. gordonii* (g) and *P. gingivalis* (h) biofilms. Data are presented as mean ± SD, ***$P < 0.001$, ****$P < 0.0001$, ns denotes no significant difference.

Open Access Article. Published on 02 January 2026. Downloaded on 1/20/2026 9:03:54 PM.
This article is licensed under a Creative Commons Attribution-NonCommercial 3.0 Unported Licence.

fluorescence with a smaller proportion of red fluorescence, suggesting that only a small fraction of the bacteria were dead. In contrast, the biofilms of *S. gordonii* and *P. gingivalis* in the 2TT-oC6B@LIP + L group were predominantly stained red (indicating dead bacteria) by propidium iodide (PI), demonstrating that 2TT-oC6B@LIP + L exhibited excellent anti-biofilm efficiency. Statistical analysis of the percentage of dead and alive bacteria in the biofilm, as shown in Fig. 3(g) and (h), revealed that the proportion of dead bacteria was significantly higher in the 2TT-oC6B@LIP + L group ($P < 0.05$). This indicates that the photothermal therapy mediated by 2TT-oC6B@LIP has superior anti-biofilm therapeutic efficacy.

3.7 *In vitro* biosafety

Fig. 4(a) and (b) demonstrate the staining patterns of L929 cells treated with 2TT-oC6B@LIP and 2TT-oC6B@LIP + L on days 1 and 3. The results indicate that the cellular morphology of L929 cells remained largely unaltered across the entire concentration range of 2TT-oC6B@LIP and 2TT-oC6B@LIP + L tested in this

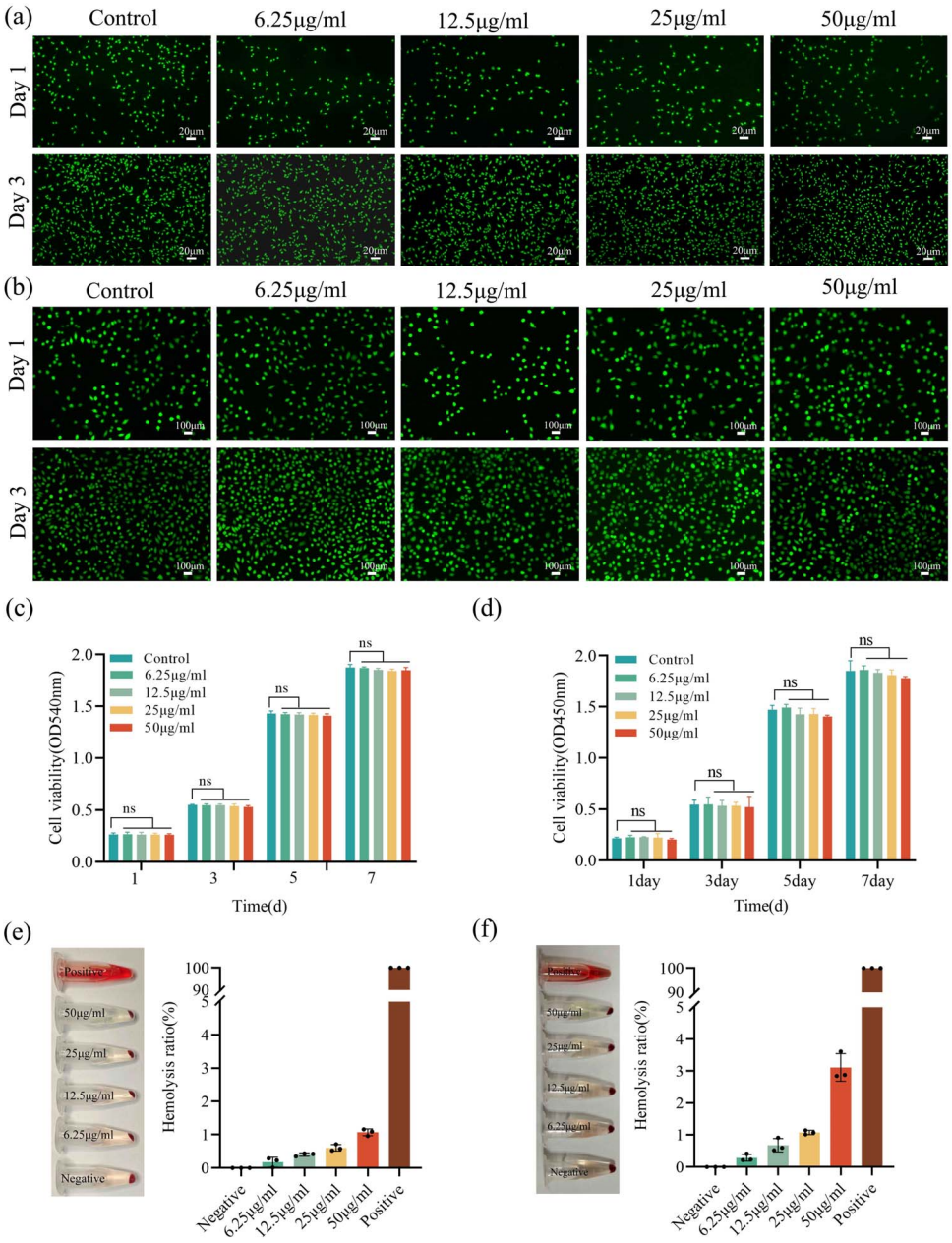

Fig. 4 *In vitro* biocompatibility of 2TT-oC6B@LIP. (a) The morphological changes of L929 cells treated with varying concentrations of 2TT-oC6B@LIP were observed on day 1 and day 3, scale bar = 20 μm. (b) Morphological alterations in L929 cells observed at day 1 and day 3 post-exposure to NIR irradiation with varying concentrations of 2TT-oC6B@LIP, scale bar = 100 μm. The survival rate of L929 cells was assessed using the CCK-8 assay after 7 days of treatment with different concentrations of 2TT-oC6B@LIP. (c) and 2TT-oC6B@LIP + L (d). Hemolysis in the dark (e). or under NIR irradiation (f). Hemolysis picture (left), hemolysis rate (right). The light irradiation parameters were 808 nm laser irradiation of 1 W cm^{-2} for 5 min. Data are presented as mean ± SD, and ns denotes no significant difference.

 © 2026 The Author(s). Published by the Royal Society of Chemistry

Open Access Article. Published on 02 January 2026. Downloaded on 1/20/2026 9:03:54 PM.
This article is licensed under a Creative Commons Attribution-NonCommercial 3.0 Unported Licence.

study, including the highest concentration of 50 μg ml^{-1}. Fig. 4(c) presents the dark toxicity evaluation of 2TT-oC6B@LIP on L929 cells over 7 days. The cell viability assessment revealed no significant changes in cellular viability with increasing concentrations of 2TT-oC6B@LIP nanoparticles compared to the control group throughout the 1-, 3-, 5-, and 7-day co-incubation periods ($P > 0.05$). The impact of light irradiation on cell viability was further evaluated, as shown in Fig. 4(d). At a concentration of 50 μg ml^{-1}, the 2TT-oC6B@LIP + L group showed a marginally reduced cell survival rate compared to the control group and other treatment groups. However, this difference did not reach statistical significance ($p > 0$ 0.05). The findings confirm that 2TT-oC6B@LIP maintains high biocompatibility and biosafety with L929 cells, irrespective of light exposure.

In addition, the hemolytic toxicity of 2TT-oC6B@LIP and 2TT-oC6B@LIP + L was assessed across a concentration range of 6.25–50 μg ml^{-1}, with the results presented in Fig. 4(e) and (f). The positive control group exhibited significant erythrocyte destruction and hemoglobin leakage, whereas no notable hemolysis was observed in the experimental groups. It is noteworthy that even at the highest concentration tested (50 μg ml^{-1}), the hemolysis rates remained minimal, with 2TT-oC6B@LIP exhibiting only 1.07% ± 0.08% and 2TT-oC6B@LIP + L showing a slightly higher but still low value of 3.11% ± 0.35%. These results collectively demonstrate that 2TT-oC6B@LIP and 2TT-oC6B@LIP + L nanoparticles exhibit excellent hemocompatibility.

3.8 *In vivo* assessment of photothermal antimicrobial efficacy

As illustrated in Fig. 5(a), we established an experimental periodontitis model in SD rats using the ligation technique to assess

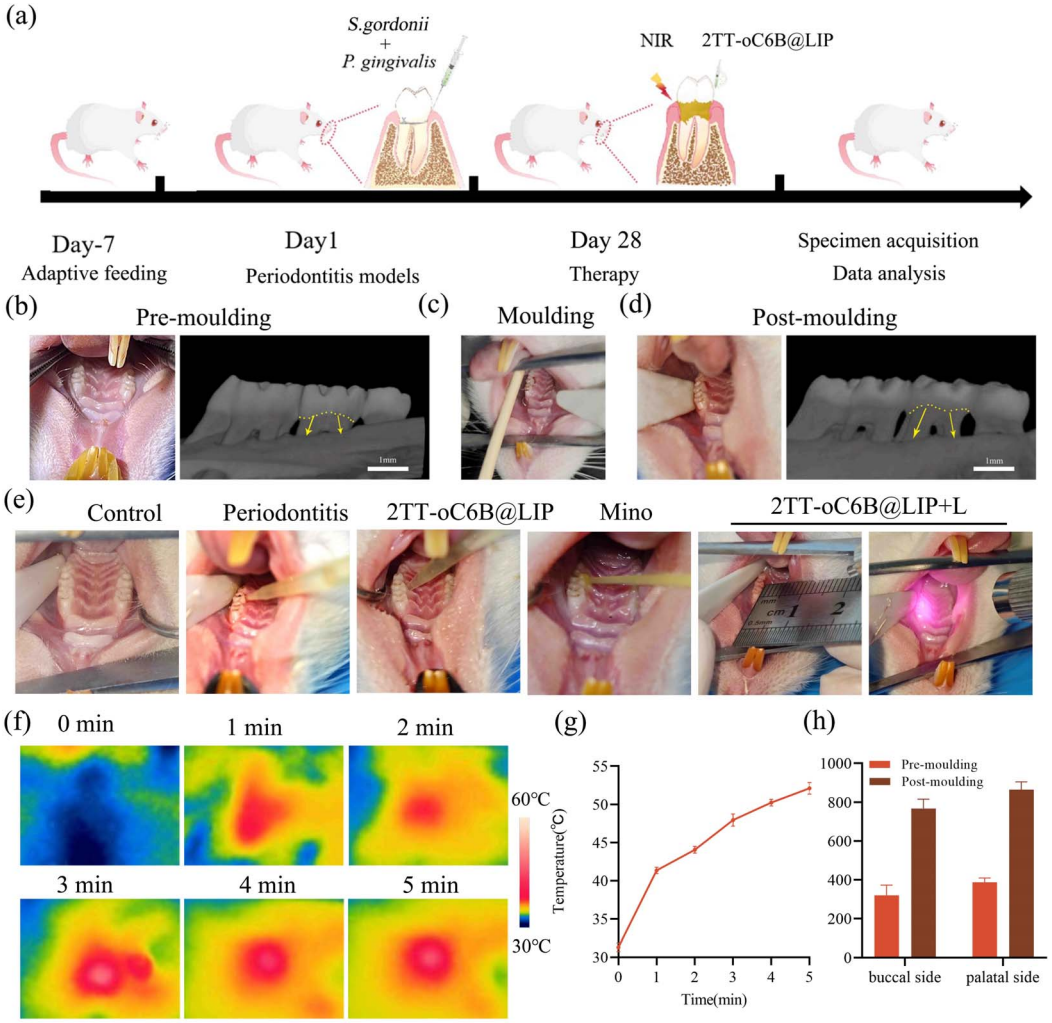

Fig. 5 The therapeutic course of 2TT-oC6B@LIP in a rat model of periodontitis. (a) Schematic diagram illustrating the experimental protocol for establishing the SD rat periodontitis model. (b) Intraoral (left) and Micro-CT(right) images of rats before modeling, scale bar = 1 μm. (c) Intraoral image of a rat ligature modeling (d) Intraoral (left) and Micro-CT (right) images of rats after modeling, scale bar = 1 μm. (e) Intraoral images of rats after different treatments. (f) Time-series intraoral thermographic images (scale bar: 30–60 °C) captured within a 5-minute monitoring window. (g) Quantitative analysis of intraoral temperature fluctuations during the 5-minute observation period. (h) Amount of buccolingual alveolar bone loss in rats before and after modelling. Data are presented as mean ± SD.

Open Access Article. Published on 02 January 2026. Downloaded on 1/20/2026 9:03:54 PM.
This article is licensed under a Creative Commons Attribution-NonCommercial 3.0 Unported Licence.

the photothermal bactericidal efficacy of 2TT-oC6B@LIP under NIR light irradiation (1 W cm^{-2} for 5 minutes). Fig. 5(b–d) presents a comprehensive visualization of the intraoral changes throughout the experimental timeline, encompassing pre-modeling, modeling, and post-modeling stages. Comparative analysis revealed pronounced gingival inflammation in modeled rats, characterized by marked erythema and edema after four weeks of modeling, in contrast to the healthy gingival architecture observed in control animals. Micro-CT imaging further confirmed the successful establishment of the periodontitis model, demonstrating substantial alveolar bone resorption in the experimental group. As shown in Fig. 5(h), alveolar bone loss in the modeling group was approximately twice that of the control group.

Following the four-week modeling period, the ligature wire was removed, and experimental rats were subjected to their respective therapeutic interventions according to the predetermined group allocations, as visually documented in Fig. 5(e). NIR light irradiation in the 2TT-oC6B@LIP + L group was accurately targeted to the periodontitis lesion margins without causing any detectable adverse effects to adjacent healthy tissues As illustrated in Fig. 5(f), to monitor temperature variations within the periodontal pockets, 2TT-oC6B@LIP was administered *via* local injection followed by near-infrared

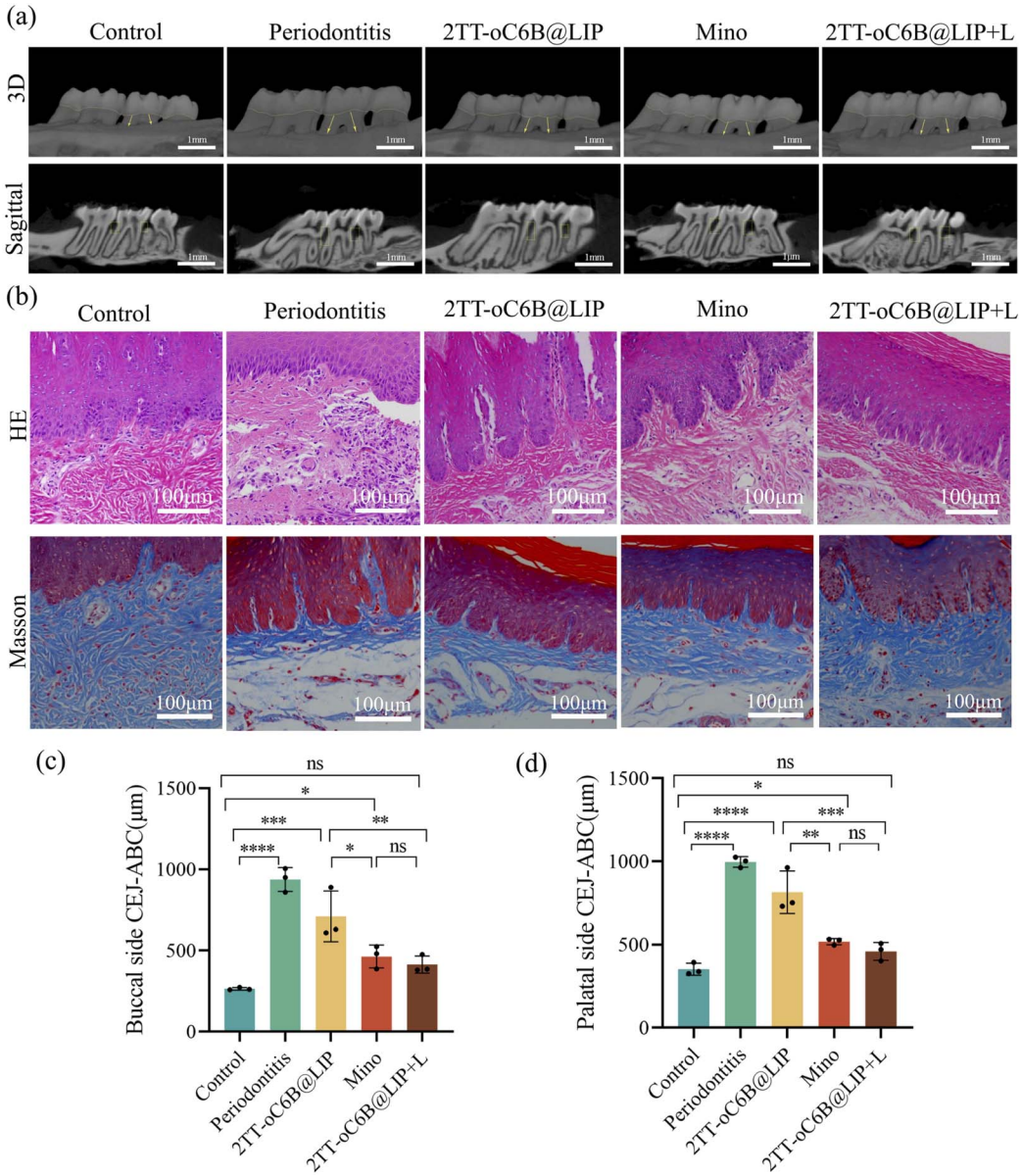

Fig. 6 Therapeutic efficacy of 2TT-oC6B@LIP in a rat model of periodontitis. (a) Three-dimensional reconstruction of the maxillary alveolar bone architecture with corresponding cross-sectional Micro-CT images; the yellow dashed line demarcates the enamel–cement junction, while the yellow arrow indicates the linear measurement from CEJ to ABC, scale bar = 1 μm. (b) Representative photomicrographs of H&E- and Masson's trichrome-stained periodontal tissues from experimental groups, scale bar = 100 μm. Quantitative analysis of alveolar bone loss at buccal. (c) and palatal (d) aspects. Data are presented as mean ± SD, *$P < 0.05$,**$P < 0.01$,***$P < 0.001$, ****$P < 0.0001$, ns denotes no significant difference.

 © 2026 The Author(s). Published by the Royal Society of Chemistry

Open Access Article. Published on 02 January 2026. Downloaded on 1/20/2026 9:03:54 PM.
This article is licensed under a Creative Commons Attribution-NonCommercial 3.0 Unported Licence.

irradiation for 5 minutes, with continuous thermal monitoring using an infrared imaging system. Quantitative thermal analysis, presented in Fig. 5(g), demonstrated that the 2TT-oC6B@LIP + L group achieved a maximum gingival temperature of 52.9 °C while maintaining tissue integrity and causing no observable damage to surrounding healthy tissues.[49] These findings suggest that 2TT-oC6B@LIP + L has an excellent photothermal effect.

In Fig. 6(a), alveolar bone loss was quantified by measuring the vertical distance between the alveolar bone crest (ABC) of the maxillary second molar and the cementoenamel junction (CEJ). In the SD rat periodontitis model, alveolar bone loss is the

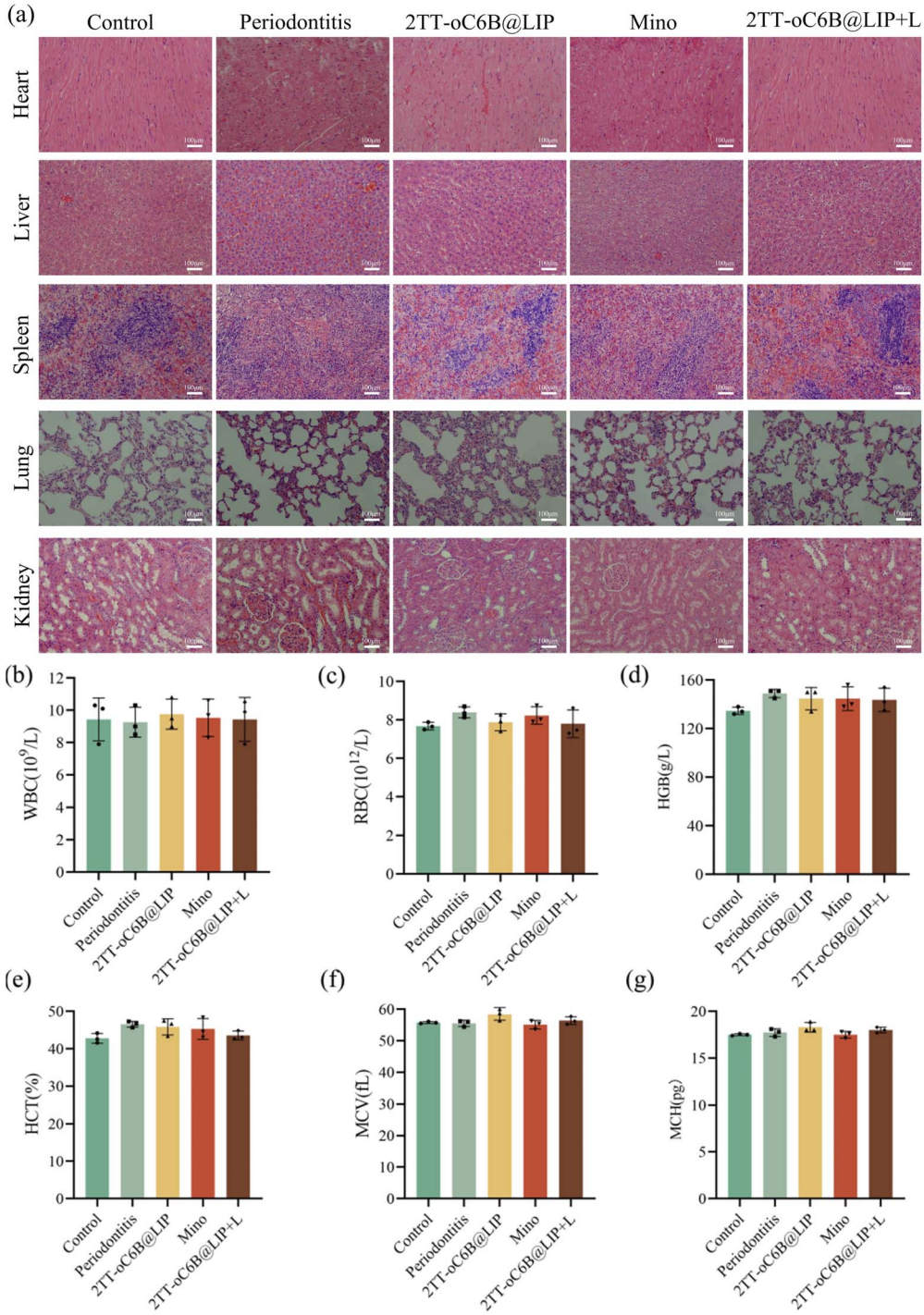

Fig. 7 *In vivo* biosafety assessment of 2TT-oC6B@LIP. (a) Hematoxylin and eosin staining of major organs was performed on SD rats receiving different treatments, scale bar = 100 μm. Hematological parameters were examined in SD rats after different treatments, including white blood cells (b), red blood cells (c), concentration of hemoglobin (d), hematocrit count (e), mean corpuscular volume (f), and mean corpuscular hemoglobin (g). Data are presented as mean ± SD.

Open Access Article. Published on 02 January 2026. Downloaded on 1/20/2026 9:03:54 PM.
This article is licensed under a Creative Commons Attribution-NonCommercial 3.0 Unported Licence.

most direct and critical indicator of disease severity and treatment efficacy. The rats were evaluated according to their respective treatment groups. The results, presented in Fig. 6(c) and 5(d), showed that both the 2TT-oC6B@LIP and Mino groups exhibited reduced buccal and palatal ABC-CEJ distances compared to the Periodontitis group (0.93 ± 0.07 mm and 1.06 ± 0.10 mm, respectively). Notably, the 2TT-oC6B@LIP + L group demonstrated the smallest buccal and palatal ABC-CEJ distances (0.41 ± 0.04 mm and 0.46 ± 0.05 mm, respectively), which were not statistically different from the control group ($P > 0.05$). These findings indicate that the 2TT-oC6B@LIP + L treatment significantly reduced alveolar bone loss.

The pathogenesis of periodontitis involves bacterial biofilm accumulation, which triggers host inflammatory cell recruitment and subsequent inflammatory cascade activation.[50,51] Histopathological evaluation of the gingival tissues adjacent to the maxillary second molar was performed using H&E staining, as presented in Fig. 6(b). Microscopic analysis revealed distinct morphological differences among experimental groups: the Control group maintained normal gingival architecture, while the periodontitis and 2TT-oC6B@LIP groups exhibited characteristic pathological features, including epithelial hyperplasia, connective tissue disorganization, and significant inflammatory cell infiltration. Notably, the Mino group demonstrated moderate improvement in inflammatory status, whereas the 2TT-oC6B@LIP + L group showed near-normal tissue architecture with well-organized epithelial alignment and minimal inflammatory cell presence.

Collagen fibers represent essential structural components of periodontal tissues, serving as critical targets for periodontal pathogens through collagenase-mediated degradation.[52] To evaluate collagen organization and periodontal regeneration, Masson's trichrome staining was employed for histological assessment. As demonstrated in Fig. 6(b), comparative analysis revealed distinct therapeutic outcomes: the Mino group exhibited moderate improvement in periodontal soft tissue repair, while the 2TT-oC6B@LIP + L group displayed optimal collagen regeneration, characterized by well-organized, densely packed collagen deposition (evidenced by blue reticulated fibrous structures). In contrast, the Periodontitis group showed characteristic pathological features of collagen disorganization, with loosely arranged and fragmented fibers. These findings suggest that 2TT-oC6B@LIP + L treatment significantly enhances collagen remodeling and deposition, thereby promoting periodontal tissue regeneration.

3.9 Histological examination of *in vivo* biosafety

To evaluate the potential systemic toxicity of 2TT-oC6B@LIP + L, comprehensive hematological analysis and histopathological examination were conducted. Histopathological assessment, presented in Fig. 7(a), revealed normal tissue architecture in major organs (including heart, liver, spleen, lungs, and kidneys) across all experimental groups. Microscopic examination showed the absence of pathological alterations, inflammatory cell infiltration, or tissue damage, confirming the biocompatibility of 2TT-oC6B@LIP + L. Fig. 7(b–g) illustrates that abdominal aortic blood samples were collected from experimental animals for complete blood count analysis. Hematological parameters across all treatment groups remained within normal physiological ranges and showed no statistically significant differences compared to the control group, demonstrating the favorable biosafety profile of 2TT-oC6B@LIP + L. These collective findings strongly support the clinical translational potential of 2TT-oC6B@LIP + L as a safe therapeutic agent. While short-term data support favorable biosafety, comprehensive studies on long-term toxicity, clearance, and systemic effects remain essential for future clinical development.

4. Conclusions

In conclusion, this study successfully developed an innovative antimicrobial platform by encapsulating 2TT-oC6B, an AIE material with NIR-II photothermal properties, into liposomes through nanoprecipitation. The resulting 2TT-oC6B@LIP demonstrated remarkable efficacy in periodontitis treatment, exhibiting potent antibacterial activity against periodontal pathogens under NIR light irradiation (808 nm, 1 W cm^{-2}). ONPG and BCA assays performed on *S. gordonii* and *P. gingivalis* confirmed that 2TT-oC6B@LIP disrupts the bacterial membrane barrier, leading to increased permeability and subsequent protein leakage, ultimately causing bacterial cell death. The system effectively eradicated periodontal plaque biofilms while maintaining excellent cytocompatibility and hemocompatibility, suggesting its strong potential for clinical applications. Critically, the therapeutic efficacy of 2TT-oC6B@LIP was robustly validated in a ligature-induced periodontitis model in SD rats employing a polymicrobial challenge with these two key periodontopathogens. The treatment significantly inhibited disease progression while maintaining an optimal biosafety profile, presenting a promising therapeutic strategy against periodontal drug-resistant bacteria through photothermal therapy. Future studies may explore its application in even more complex multispecies environments to further simulate the full intricacy of human periodontal disease.

Despite these encouraging outcomes, several limitations warrant consideration. The non-specific antibacterial activity of the NIR-II irradiation, while beneficial for broad-spectrum efficacy, may potentially disrupt the balance of the normal periodontal microflora. In this context, the work of Wang's team offers a promising direction: through the rational design of poly(dopamine)-based nanostructures—from coated Prussian blue nanozymes (PPM NPs) to a core–satellite system (PPAg) with integrated silver satellites—they established a targeted strategy for eradicating periodontal pathogens that circumvents the ecological drawbacks of conventional photothermal therapy. Such integrated platforms highlight the potential of synergistic combination approaches in addressing selectivity challenges.[53,54] Furthermore, the therapeutic efficacy of photothermal therapy depends critically on precise control of irradiation parameters, as suboptimal selection of light power, exposure duration, or source-to-tissue distance could compromise treatment outcomes or cause collateral tissue damage.

 © 2026 The Author(s). Published by the Royal Society of Chemistry

Open Access Article. Published on 02 January 2026. Downloaded on 1/20/2026 9:03:54 PM.
This article is licensed under a Creative Commons Attribution-NonCommercial 3.0 Unported Licence.

Inspired by these advances, future research should focus on developing multimodal treatment regimens that combine mild photothermal therapy with photodynamic therapy and fluorescence imaging, thereby achieving spatiotemporal control and enhancing overall therapeutic precision in periodontal applications.

In summary, clinical translation of these technologies requires overcoming several challenges, particularly in developing targeted antimicrobial strategies and optimizing multimodal combination therapies. Future efforts should focus on establishing clinically relevant microbial models, precisely controlling treatment parameters, and intelligently combining photothermal therapy with other modalities to enable precise and personalized periodontal treatment.

Author contributions

Huijuan Yin: writing – review & editing, validation, supervision, project administration, methodology, conceptualization. Shisheng Cao: writing – original draft, methodology, data curation, conceptualization. Meng Xia: writing – original draft, methodology, data curation, conceptualization. Xingtong Mu: writing – original draft, methodology, data curation, conceptualization. Cailing Zhao: writing – review & editing, methodology, funding acquisition, data curation, conceptualization. Juan Zhang: writing – review & editing, supervision, project administration, funding acquisition, conceptualization. Qing Yang: writing – original draft, methodology, investigation, data curation, conceptualization.

Conflicts of interest

The authors declare that they have no known competing financial interests or personal relationships that could have appeared to influence the work reported in this paper.

Data availability

All data supporting the findings of this study, including the data for figures and tables, are included within the article.

Acknowledgements

The study was supported by the Science and Technology Project of Tianjin Municipal Health and Wellness Commission (No. TJWJ2022MS015).

References

1 J. M. Albandar, *Periodontol*, 2000, **2024**, 1–13.
2 M. X. Chen, Y. J. Zhong, Q. Q. Dong, H. M. Wong and Y. F. Wen, *J. Clin. Periodontol.*, 2021, **48**, 1165–1188.
3 S. Z. Farhad, A. Karbalaeihasanesfahani, E. Dadgar, K. Nasiri, M. Esfahaniani and M. Nabi Afjadi, *Mol. Biol. Rep.*, 2024, **51**, 814.
4 G. Hajishengallis, *Periodontol 2000*, 2022, **89**, 9–18.
5 F. S. C. Sczepanik, M. L. Grossi, M. Casati, M. Goldberg, M. Glogauer, N. Fine and H. C. Tenenbaum, *Periodontol 2000*, 2020, **84**, 45–68.
6 Q. Cao, X. Xiao, C. Tao, R. Shi, R. Lv, R. Guo, X. Li, B. Sui, X. Liu and J. Liu, *Biomater. Sci.*, 2023, **11**, 5680–5693.
7 C. A. de Jongh, T. J. de Vries, F. J. Bikker, S. Gibbs and B. P. Krom, *J. Oral Microbiol.*, 2023, **15**, 2205291.
8 A. Verma, G. Azhar, X. Zhang, P. Patyal, G. Kc, S. Sharma, Y. Che and J. Y. Wei, *Int. J. Mol. Sci.*, 2023, **24**, 950.
9 J. Luan, R. Li, W. Xu, H. Sun, Q. Li, D. Wang, S. Dong and J. Ding, *Acta Pharm. Sin. B*, 2023, **13**, 2310–2333.
10 M. Mahdizade Ari, N. Amirmozafari, D. Atieh, R. Afifirad, P. Asadollahi and G. Irajian, *Front. Chem.*, 2024, **12**, 1384344.
11 S. Huang, M. Qi and Y. Chen, *Front. Microbiol.*, 2023, **14**, 948092.
12 N. R. Kumaar and S. C. Nair, *Ther. Delivery*, 2023, **14**, 227–249.
13 L. Cao, Y. Wu, Y. Shan, B. Tan and J. Liao, *Biomed. Mater.*, 2022, **17**, 022008.
14 L. He, D. Di, X. Chu, X. Liu, Z. Wang, J. Lu, S. Wang and Q. Zhao, *J Control Release*, 2023, **363**, 180–200.
15 B. Wang, Y. Xu, D. Shao, L. Li, Y. Ma, Y. Li, J. Zhu, X. Shi and W. Li, *Front. Bioeng. Biotechnol.*, 2022, **10**, 1047598.
16 Q. Duan, J. Wang, B. Zhang, X. Wang, J. Xue, W. Zhang and S. Sang, *Colloids Surf., B*, 2022, **210**, 112247.
17 S. Yu, G. Xia, N. Yang, L. Yuan, J. Li, Q. Wang, D. Li, L. Ding, Z. Fan and J. Li, *Int. J. Mol. Sci.*, 2024, **25**, 5632.
18 Y. Ge, J. Zhang, K. Jin, Z. Ye, W. Wang, Z. Zhou and J. Ye, *Acta Biomater.*, 2023, **167**, 551–563.
19 H. Shen, C. Zhang, Y. Meng, Y. Qiao, Y. Ma, J. Chen, X. Wang and L. Pan, *Adv. Healthcare Mater.*, 2024, **13**, e2303000.
20 D. Zhang, S. Bie, M. Anas Tomeh, X. Zhang and X. Zhao, *Eur. J. Pharm. Biopharm.*, 2024, **204**, 114516.
21 D. G. García, C. Garzón-Romero, M. A. Salazar, K. J. Lagos, K. O. Campaña, A. Debut, K. Vizuete, M. R. Rivera, D. Niebieskikwiat, M. J. Benitez and M. P. Romero, *Int. J. Mol. Sci.*, 2023, **24**, 4770.
22 X. Qiu, L. Nie, P. Liu, X. Xiong, F. Chen, X. Liu, P. Bu, B. Zhou, M. Tan, F. Zhan, X. Xiao, Q. Feng and K. Cai, *Biomaterials*, 2024, **308**, 122548.
23 R. Li, C. Liu, C. Wan, T. Liu, R. Zhang, J. Du, X. Wang, X. Jiao, R. Gao and B. Li, *Int. J. Nanomed.*, 2023, **18**, 3309–3324.
24 R. Li, C. Wan, Y. Li, X. Jiao, T. Liu, Y. Gu, R. Gao, J. Liu and B. Li, *Colloids Surf., B*, 2024, **244**, 114179.
25 X. Guo, L. Li, W. Jia, C. Zhang, W. Ren, C. Liu and Y. Tang, *ACS ApplACS Appl. Mater. Interfaces. Mater. Interfaces*, 2024, **16**, 19926–19936.
26 J. Li, G. Pan, G. V. Zyryanov, Y. Peng, G. Zhang, L. Ma, S. Li, P. Chen and Z. Wang, *ACS ApplACS Appl. Mater. Interfaces. Mater. Interfaces*, 2023, **15**, 40864–40876.
27 M. Kim, J. E. Hwang, J. S. Lee, J. Park, C. Oh, S. Lee, J. Yu, W. Zhang and H. J. Im, *ACS ApplACS Appl. Mater. Interfaces. Mater. Interfaces*, 2024, **16**, 32945–32956.
28 G. Yang, R. Fan, J. Yang, L. Yi, S. Chen and W. Wan, *Biomaterials*, 2023, **302**, 122347.
29 B. Zhao, H. Wang, W. Dong, S. Cheng, H. Li, J. Tan, J. Zhou, W. He, L. Li, J. Zhang, G. Luo and W. Qian, *J. Nanobiotechnol.*, 2020, **18**, 137.

Open Access Article. Published on 02 January 2026. Downloaded on 1/20/2026 9:03:54 PM.
This article is licensed under a Creative Commons Attribution-NonCommercial 3.0 Unported Licence.

30 Y. Zhao, Y. Wang, X. Wang, R. Qi and H. Yuan, *Nanomaterials*, 2023, **13**, 2269.
31 F. Hu, S. Xu and B. Liu, *Adv. Mater.*, 2018, **30**, e1801350.
32 Y. Li, Z. Cai, S. Liu, H. Zhang, S. T. H. Wong, J. W. Y. Lam, R. T. K. Kwok, J. Qian and B. Z. Tang, *Nat. Commun.*, 2020, **11**, 1255.
33 J. Luo, Z. Xie, J. W. Lam, L. Cheng, H. Chen, C. Qiu, H. S. Kwok, X. Zhan, Y. Liu, D. Zhu and B. Z. Tang, *Chem. Commun.*, 2001, 1740–1741, DOI: 10.1039/b105159h.
34 H. Chen, P. Bao, Y. Lv, R. Luo, J. Deng, Y. Yan, D. Ding and H. Gao, *ACS ApplACS Appl. Mater. Interfaces. Mater. Interfaces*, 2023, **15**, 56895–56908.
35 W. Wang, G. Zhang, Y. Wang, J. Ran, L. Chen, Z. Wei, H. Zou, Y. Cai and W. Han, *J. Nanobiotechnol.*, 2023, **21**, 367.
36 D. Yan, Y. Huang, J. Zhang, Q. Wu, G. Song, J. Ji, Q. Jin, D. Wang and B. Z. Tang, *J. Am. Chem. Soc.*, 2023, **145**, 25705–25715.
37 J. Du, S. Liu, P. Zhang, H. Liu, Y. Li, W. He, C. Li, J. H. C. Chau, R. T. K. Kwok, J. W. Y. Lam, L. Cai, Y. Huang, W. Zhang, J. Hou and B. Z. Tang, *ACS ApplACS Appl. Mater. Interfaces. Mater. Interfaces*, 2020, **12**, 8040–8049.
38 S. J. Liu, C. Chen, Y. Y. Li, H. K. Zhang, J. K. Liu, R. Wang, S. T. H. Wong, J. W. Y. Lam, D. Ding and B. Tang, *Adv. Funct. Mater.*, 2020, **30**, 10.
39 X. Cheng, J. Gao, Y. Ding, Y. Lu, Q. Wei, D. Cui, J. Fan, X. Li, E. Zhu, Y. Lu, Q. Wu, L. Li and W. Huang, *Adv. Sci.*, 2021, **8**, e2100876.
40 W. Gao, L. Li, X. Zhang, L. Luo, Y. He, C. Cong and D. Gao, *Nanomedicine*, 2020, **15**, 871–890.
41 D. E. Large, R. G. Abdelmessih, E. A. Fink and D. T. Auguste, *Adv. Drug Delivery Rev.*, 2021, **176**, 113851.
42 R. Binaymotlagh, F. Hajareh Haghighi, L. Chronopoulou and C. Palocci, *Gels*, 2024, **10**, 284.
43 N. G. Shetake, M. Ali, A. Kumar, J. Bellare and B. N. Pandey, *Biomater. Adv.*, 2022, **142**, 213147.
44 G. Chen, L. Wang, P. He, T. Su, Q. Lai, H. C. Kuo, W. Wu, S. L. Chen and C. C. Tu, *ACS Appl. Bio Mater.*, 2023, **6**, 4856–4866.
45 Y. Yang, P. He, Y. Wang, H. Bai, S. Wang, J. F. Xu and X. Zhang, *Angew Chem. Int. Ed. Engl.*, 2017, **56**, 16239–16242.
46 L. Feng, C. Peillex-Delphe, C. Lü, D. Wang, S. Giannakis and C. Pulgarin, *Water Res.*, 2020, **182**, 116049.
47 M. Zhang, Y. Yu, L. Lian, W. Li, J. Ren, Y. Liang, F. Xue, F. Tang, X. Zhu, J. Ling and J. Dai, *Probiotics Antimicrob. Proteins*, 2022, **14**, 169–179.
48 H. Qiu, F. Pu, Z. Liu, Q. Deng, P. Sun, J. Ren and X. Qu, *Small*, 2019, **15**, e1902522.
49 E. Shi, L. Bai, L. Mao, H. Wang, X. Yang, Y. Wang, M. Zhang, C. Li and Y. Wang, *J. Nanobiotechnol.*, 2021, **19**, 413.
50 A. A. Abdulkareem, F. B. Al-Taweel, A. J. B. Al-Sharqi, S. S. Gul, A. Sha and I. L. C. Chapple, *J. Oral Microbiol.*, 2023, **15**, 2197779.
51 Q. Chen, M. Qi, F. Shi, C. Liu, Y. Shi, Y. Sun, X. Bai, L. Wang, X. Sun, B. Dong and C. Li, *Adv. Healthcare Mater.*, 2023, **12**, e2300313.
52 Y. Wang, H. N. Su, H. Y. Cao, S. M. Liu, S. C. Liu, X. Zhang, P. Wang, C. Y. Li, Y. Z. Zhang, X. Y. Zhang and X. L. Chen, *Appl. Environ. Microbiol.*, 2022, **88**, e0167721.
53 P. Wang, L. Wang, Y. Zhan, Y. Liu, Z. Chen, J. Xu, J. Guo, J. Luo, J. Wei, F. Tong and Z. Li, *Chem. Eng. J.*, 2023, **463**, 142293.
54 P. Wang, L. Wang, Y. Liu, Y. Mu, Y. Deng, A. Jia, Y. Zhan, J. Guo, Z. Li and F. Tong, *ACS ApplACS Appl. Mater. Interfaces. Mater. Interfaces*, 2025, **17**, 47969–47984.

 © 2026 The Author(s). Published by the Royal Society of Chemistry